


APPROVAL SHEET

Title of Thesis: Modeling the pathogenesis of early-stage atherosclerosis following ionizing radiation exposure: A three-dimensional numerical study using COMSOL

Name of Candidate: Ann Marie K. Weideman
Master of Science in Applied Mathematics, 2016

Thesis and Abstract Approved: _____


(Dr. Bradford Peercy)
(Associate Professor)
(Mathematics and Statistics)

Date Approved: April 29, 2016

NOTE: *The Approval Sheet with the original signature must accompany the thesis or dissertation. No terminal punctuation is to be used.

ABSTRACT

Title of Thesis: Modeling the pathogenesis of early-stage atherosclerosis following ionizing radiation exposure: A three-dimensional numerical study using COMSOL

Ann Marie K. Weideman, Master of Science, 2016

Thesis directed by:

Dr. Bradford E. Peercy, Associate Professor, Department of Mathematics and Statistics, University of Maryland, Baltimore County

Dr. Mark P. Little, Senior Investigator, Radiation Epidemiology Branch, Division of Cancer Epidemiology and Genetics, National Cancer Institute

According to a World Health Organization 2012 report, ischemic heart disease and stroke top the list of the ten leading causes of death in the world. Atherosclerosis, a major cause of both diseases, initiates with damage to the endothelium of the arterial wall and leads to the formation of plaque buildup within the artery. Many lifestyle factors contribute to the development of atherosclerosis including history of hypertension, smoking, and high cholesterol. Less investigated is the contribution of radiation-induced cellular death in the initiation of atheroma. This research is a continuation of a 2009 study [1] in which Little *et al.* developed a nonlinear system of reaction-diffusion equations on a 2D annulus to model cardiovascular disease after low-dose radiation exposure. However, this model was limited due to simplifications in the biology and due to system instabilities, as the concentration of several species blew up after brief perturbation. We used COMSOL Multiphysics v. 4.4 [2], a finite element analysis software package, to resolve any system

instabilities and introduce cell survival curves within the initial conditions. The results of this model can be used to predict the rate of lesion formation hours or days post-exposure in those exposed to radiological incidents (e.g. nuclear facility breach or terrorism) or therapeutic doses of ionizing radiation. Our work found that there is an increase in plaque size, and thus increased risk of an adverse cardiac event, associated with absorbed doses of greater than or equal to 2.2 Gray (Gy). These results have tremendous implications on current radiotherapy routines, which typically employ daily conventional or hypofractionated doses of 1.8-2.0 Gy, but can deliver upwards of 2.0 Gy for certain regimens. We expect that investigators and medical professionals will be able to modify the radiation dose and time scale in order to determine the effects on nine different phenomena involved in the initiation of atherosclerosis.

Modeling the pathogenesis of early-stage atherosclerosis following ionizing
radiation exposure: A three-dimensional numerical study using COMSOL

by

Ann Marie Weideman

Thesis submitted to the Faculty of the Graduate School of the University of Maryland,
Baltimore County in partial fulfillment of the requirements for the degree of Master of
Science in Applied Mathematics, 2016

This Thesis is Dedicated to:

Nathan P. Weideman

&

Ann K. Dowling

ACKNOWLEDGEMENTS

I would like to thank my UMBC mentor Dr. Bradford E. Peercy for guiding me through the past eight months of work and NIH mentor Dr. Mark P. Little for suggesting possible thesis topics.

I would also like to thank Dr. Kathleen Hoffman and Dr. Hye-Won Kang for edits and helpful suggestions in preparation of this manuscript.

Finally, I would like to thank the National Institutes of Health, Biomedical Research Training Program for the grant support of this and other projects.

TABLE OF CONTENTS

	Page
DEDICATION.....	ii
ACKNOWLEDGEMENTS	iii
LIST OF FIGURES	v
CHAPTER	
1 INTRODUCTUTORY BACKGROUND.....	1
1.1 Pathogenesis of Atherosclerosis	1
2 MATERIALS AND METHODS.....	3
2.1 Parameters and Software	3
2.2 Geometry of the Human Coronary Artery	3
2.3 Reaction-Diffusion System in General Form	4
2.4 Initial Conditions	7
2.5 Boundary Conditions	10
2.6 Time-Dependent Solver	11
3 RESULTS	12
3.1 Time Scale and Absorbed Dose	12
3.2 Graphical Results	12
4 DISCUSSION	20
4.1 Findings and Limitations	20
4.2 Radiological Implications	21
APPENDIX	24
BIBLIOGRAPHY	29

LIST OF FIGURES

FIGURE	Page
2.2.1. Cross-section and numerical finite element discretization of the artery. A) Lumen (1) with diameter 2.20×10^{-3} mm, arterial wall (2) with total thickness of 8.35×10^{-1} mm (intima = 2.35×10^{-1} mm, media = 2.00×10^{-1} mm, adventitia = 4.00×10^{-1} mm), and epicardial adipose tissue (3) with thickness 5.00 mm. B) Physics-controlled mesh with normal element size for artery segment (see section 2.6 for further details).	4
2.4.1. The surviving fraction of undamaged endothelial cells, monocytes, and T-cells after a single dose of ionizing radiation.	10
3.2.1. Monocyte and T-cell response to varied doses (2.1-2.7 Gy) of ionizing radiation (administered at $t = 0$ h). As can be visualized by the abrupt increase in immune cells, the chemoattractant threshold is surpassed at approximately 2.2 Gy.	15
3.2.2 The effect of single doses of ionizing radiation (administered at $t = 0$ h) on the concentrations of nine species involved in atheroma development 0 – 90 seconds (left panel) and 0 – 6 hours (right panel) post-radiation. (A, B) Undamaged and (C, D) damaged endothelial cell concentrations as a function of time after exposure. (E, F) Chemoattractant (MCP-1), (G, H) proliferation factor (M-CSF), (I, J) monocyte, (K, L) macrophage, (M, N) macrophage-bound lipid, (O, P) T-cell, and (Q, R) necrotic core cocentrations as a function of time after exposure.	16
3.2.3 Intima cross sections at four different time points (A) 0 s (B) 180 s (C) 1800 s (D) 5400 s. The concentration of MCP-1 (color-coded) after 5 Gy rapidly reaches peak value within 180 s and then slowly decays to threshold ($2.16\text{E-}8 \text{ mol/m}^3$) at 5400 seconds (1.5 hour).	19
A.1 (A) Estimate of relative error at each iteration for a convergence criterion of $1\text{E-}7$. (B) Convergence of the time-dependent solver for varied absorbed doses.	28

CHAPTER 1

INTRODUCTORY BACKGROUND

Atherosclerosis often starts early in life and can progress silently without clinical manifestation until severe and life-threatening blockages occur [3]. Although the exact cause is unknown, initiation of atheroma can be attributed to a variety of factors including endothelial cell damage and accumulation of oxidized low-density lipoprotein (oxLDL) and associated inflammatory processes in the intima (the innermost layer of the artery) [4-7]. Radiation exposure is believed to contribute to the early onset of cardiovascular disease through DNA damage and inflammation of the exposed tissue [8].

1.1 Pathogenesis of Atherosclerosis

The pathogenesis of atherosclerosis is initiated by injury to the endothelial tissue of medium or large-sized arteries, such as those of the brain, neck, heart, or legs [9]. In the case of radiation-induced injury, it is believed that the endothelium suffers the brunt of the injury, as the endothelial cells are highly sensitive to DNA damage [10]. This damage can occur in the form of single or double-stranded breaks, base damage, or covalent cross-linking of proteins to the DNA [11]. The arterial wall eventually develops a “leaky spot,” which permits the influx of low-density lipoprotein (LDL) into the intima and subsequent oxidation of the lipid by a reactive oxygen species (ROS) to form oxLDL [1]. Post-radiation damage to the endothelium increases with growing oxLDL concentration [1], and dysfunctional cells release proteins including proliferation factor (e.g. macrophage colony-stimulating factor (M-CSF)) and chemokines (e.g. monocyte chemo-attractant protein-1 (MCP-1)). M-CSF induces the differentiation of intimal monocytes to macrophages, and

MCP-1 recruits monocytes and T-cells to the arterial wall [12, 13]. The influx of monocytes and T-cells into the intima is dependent on a threshold level of MCP-1, below which there is assumed to be zero flux [14].

Atherosclerotic plaque continues to develop as the macrophages retain lipid (forming foam cells) and produce proinflammatory cytokines [15], which enhance receptor activity and promote further LDL trafficking into the intima [16]. The accumulation of dead macrophages, foam cells, and smooth muscle cells contribute to the growth of the necrotic core (lipid-rich region of necrosis within the plaque) and increase its vulnerability to rupture [17]. The plaque initially expands into the media (middle layer of the artery) before it begins to slowly occlude the artery and inhibit local blood flow [18]. Our model investigates the early-stages of atherosclerosis and does not consider the mechanical stress applied by plaque growth, resulting deformation of the membrane, or changes in laminar flow. However, the geometry was constructed to include all three layers (intima, media, and adventitia), as shown in Figure 2.2.1, with surrounding adipose tissue and a laminar flow module so that the model could eventually be modified to incorporate later stages of the disease.

CHAPTER 2

MATERIALS AND METHODS

2.1 Parameters and Software

To complete our analyses, we gathered a list of parameters (see Appendix) from a variety of peer-reviewed sources, including values from the preceding work [1]. These values were imported into COMSOL Multiphysics v. 4.4. [2], a finite element analysis software, where they were converted to international system (SI) units. We modeled our system in three-dimensions using a time dependent study within the General Form PDE and Laminar Flow interfaces.

2.2 Geometry of the Human Coronary Artery

The left and right coronary arteries, which originate from the ascending aorta, traverse the pericardium (outer membrane of the heart) and supply blood to the surrounding tissue [19]. In general, the arterial wall consists of three concentric layers: inner (intima), middle (media), and outer (adventitia). Many texts include the single-celled endothelial lining, which is in direct contact with the blood flow, as a member of the intimal layer [20-22]. We followed suit in our model and created a 15 mm-long segment of coronary artery to include the lumen (channel where blood flow occurs), arterial wall, and surrounding epicardial adipose tissue [23], as seen in Figure 2.2.1. As previously indicated, we constructed our model to scale for future elaboration on this study.

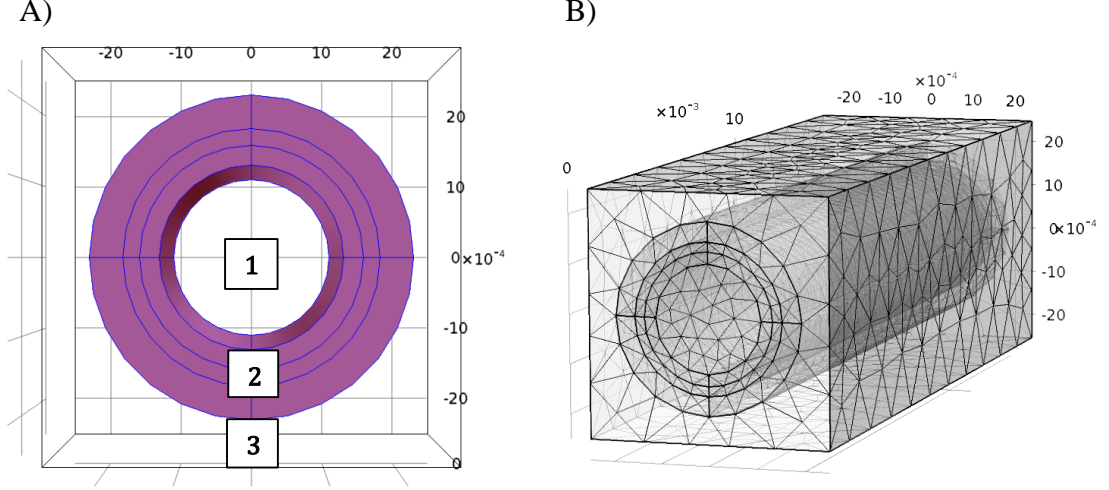


Figure 2.2.1. Cross-section and numerical finite element discretization of the artery. A) Lumen (1) with diameter 2.20×10^{-3} mm, arterial wall (2) with total thickness of 8.35×10^{-1} mm (intima = 2.35×10^{-1} mm, media = 2.00×10^{-1} mm, adventitia = 4.00×10^{-1} mm), and epicardial adipose tissue (3) with thickness 5.00 mm. B) Physics-controlled mesh with normal element size for artery segment (see section 2.6 for further details).

2.3 Reaction-Diffusion System in General Form

We use the reaction-diffusion system from Little *et al.* [1], with modifications to the initial and boundary conditions, and briefly summarize the important variables and mechanisms. As a reminder, this set of coupled equations depicts early-stage processes within the intima, where atherosclerotic changes are believed to take place. We present the system in the following general form:

$$\frac{\partial \mathbf{u}}{\partial t} + \nabla \cdot \mathbf{\Gamma} = \mathbf{F} \quad (2.3.1)$$

where $\mathbf{u} = [E_0, E_1, C, P, m, M, \eta, T, N]^T$ and $\nabla = \left[\frac{\partial}{\partial x}, \frac{\partial}{\partial y}, \frac{\partial}{\partial z} \right]$, the gradient operator. In \mathbf{u} , E_0 and E_1 represent the concentrations of undamaged and damaged endothelial cells respectively, C the concentration of chemoattractant (monocyte chemoattractant protein,

MCP-1), P the concentration of proliferation factor (macrophage colony stimulating factor, M-CSF), m the concentration of monocytes, M the concentration of macrophages, η the concentration of macrophage-bound lipid, T the concentration of T-cells, and N the concentration of the necrotic core [1]. The conservative flux \mathbf{F} is represented as the following three-dimensional vector:

$$\mathbf{F} = \begin{bmatrix} \hat{x} & \hat{y} & \hat{z} \\ 0 & 0 & 0 \\ 0 & 0 & 0 \\ -D_C C_x & -D_C C_y & -D_C C_z \\ -D_P P_x & -D_P P_y & -D_P P_z \\ m\chi_m C_x - D_m m_x & m\chi_m C_y - D_m m_y & m\chi_m C_z - D_m m_z \\ M\chi_M C_x - D_M M_x & M\chi_M C_y - D_M M_y & M\chi_M C_z - D_M M_z \\ \eta\chi_M C_x - \frac{\eta D_M M_x}{M} & \eta\chi_M C_y - \frac{\eta D_M M_y}{M} & \eta\chi_M C_z - \frac{\eta D_M M_z}{M} \\ T\chi_T C_x - D_T T_x & T\chi_T C_y - D_T T_y & T\chi_T C_z - D_T T_z \\ 0 & 0 & 0 \end{bmatrix} \quad (2.3.2)$$

where D_C, D_P, D_m, D_M, D_T represent the diffusion rate of each subscripted species, and constants χ_m, χ_M, χ_T represent the chemotactic factors of each subscripted species as dependent on chemoattractant [1]. We express the directional derivative by using subscripts x, y, or z such that $[f_x, f_y, f_z] = \left[\frac{\partial f}{\partial x}, \frac{\partial f}{\partial y}, \frac{\partial f}{\partial z} \right]$ for some arbitrary species f . The source term \mathbf{F} is similarly represented in vector form as:

$$\mathbf{F} = \begin{bmatrix} \tau(E_{0ss} - E_0) - \iota_{L0}E_0L_0 \\ \iota_{L0}E_0L_0 - d_E E_1 \\ \rho_{CE}E_1 + \rho_{CM}M + \rho_{CT}T - d_{CM}MC - d_{CT}TC - d_{cm}mC \\ \rho_{PT}T \\ m[\rho_{mP} - \rho_M]P \\ \rho_M mP - d_M(\eta, M)M \\ \rho_{in}(\eta, M)ML_0 - d_M(\eta, M)\eta \\ -d_T T \\ d_M(\eta, M)[\eta + d_{MM}M] + d_T d_{TT}T \end{bmatrix} \quad (2.3.3)$$

where the macrophage mortality $d_M(\eta, M)$ and bound lipid ingestion rate $\rho_{in}(\eta, M)$ are defined as:

$$d_M(\eta, M) = d_{M0} + \frac{R_2 \eta}{M} \quad (2.3.4)$$

$$\rho_{in}(\eta, M) = \rho_{in,high} + [\rho_{in,0} - \rho_{in,high}]e^{-R_3 \eta/M} \quad (2.3.5)$$

where d_{M0} is the underlying macrophage mortality rate, R_2 and R_3 are derived scaling constants, and $\rho_{in,0}$ and $\rho_{in,high}$ are the macrophage ingestion rates of oxidized LDL at zero and high concentrations of bound lipid [1]. As the preceding work found no experimental data regarding macrophage death rate as a function of bound lipid concentration, they were assumed to have a linear relationship as demonstrated in equation (2.3.4). An exponential curve was fit to the data in Zhao *et al.* [24] to derive the ingestion rate in equation (2.3.5) [1].

In the first row of equation (2.3.3), τ is the repopulation rate of the endothelial cells, E_{0ss} is the baseline concentration of endothelial cells, ι_{L0} is the rate of damage to endothelial cells per unit concentration of oxLDL, and L_0 is the intimal oxLDL concentration. The

terms d_E , d_M , d_T represent the death/degradation rates of endothelial cells, macrophages, and T-cells respectively. In the third row, the MCP-1 production rates ρ_C are balanced by the MCP-1 degradation rates d_C per unit concentration of the second subscripted species. Similarly, ρ_{PT} is the production rate of M-CSF per unit concentration of T-cells, ρ_{mP} is the proliferation rate of monocytes per unit concentration of proliferation factor, and ρ_M is the monocyte to macrophage conversion rate. The ratio of augmentation of the necrotic core by dying macrophages and T-cells are represented by d_{MM} and d_{TT} respectively [1]. Further details regarding the above equations may be found in the supplemental text in the preceding work [1].

As an example, we can write the equation for change in monocyte concentration as a sum of three contributions:

$$\frac{\partial m}{\partial t} + \nabla \cdot [m\chi_m \nabla C] - D_m \nabla^2 m = m[\rho_{mP} - \rho_M]P \quad (2.3.6)$$

where $\nabla \cdot [m\chi_m \nabla C]$ represents an advective chemotaxis term, $D_m \nabla^2 m$ describes the diffusion of monocytes, and $m[\rho_{mP} - \rho_M]P$ is a source term.

2.4 Initial Conditions

Several cell types within the intima are sensitive to ionizing radiation, and their survival rates can be modeled as an exponential function of dose. There exists extensive theory on appropriate modeling of cell-survival curves. For example, Section 2.5 of *Basic Radiation Oncology* [25] provides a general review of target theory, and Section 2.6 compares the

available models for single and fractionated doses. We assumed a multi-target single-hit hypothesis (each of “n” sites within a cell must be hit at least once to cause cell death [26]) for a single dose of ionizing radiation administered at time zero, a process that could be effectively modeled within the initial conditions for cell types E_0 , m , and T . Macrophages can survive doses as high as 10 Gray (Gy) [27] (equivalent to approximately 1,000 CT scans to the abdomen/pelvis [28]), so their survival after a single dose of radiation is assumed to be 100%.

We define $D0$ as the dose necessary to reduce the surviving fraction of cells to 37%, where $1/D0$ is the slope of the survival curve (subscripted depending on cell type). As inspired by data from Fig. 3 of Park *et al.* [29], the surviving fraction of undamaged endothelial cells (SF_{E0}) as dependent on dose (D) can be modeled as a shouldered survival curve with zero initial slope:

$$SF_{E0} = 1 - \left(1 - e^{-\frac{D}{D0_{E0}}}\right)^n \quad (2.4.1)$$

Where n is the extrapolation number such that $n = Dq_{E0}/D0_{E0}$, and Dq is the quasi-threshold dose (a measure of shoulder width), subscripted for the undamaged endothelial cell population. See the appendix for the parameters values and accompanying sources.

In contrast to endothelial cells, T-cells and monocytes tend to follow biphasic survival curves, where a lower primary dose is required to kill a portion of the radiosensitive cells and a higher secondary dose is required to kill the remaining portion of radioresistive cells. As inspired by data from Kwan *et al.* [30, 31], the surviving fraction of monocytes (SF_m) can be described by a biphasic, shouldered survival curve with zero initial slope, and the

surviving fraction of T-cells (SF_T) can be described by a biphasic, exponential survival curve of the form:

$$SF_m = 0.25 \left[1 - \left(1 - e^{-\frac{D}{D0_{m1}}} \right)^{n1} \right] + 0.75 \left[1 - \left(1 - e^{-\frac{D}{D0_{m2}}} \right)^{n2} \right] \quad (2.4.2)$$

$$SF_T = 0.30e^{-D/D0_{T1}} + 0.70e^{-D/D0_{T2}} \quad (2.4.3)$$

where $D0_{m1}, D0_{m2}$ represent the monocyte $D0$ values for the radiosensitive ($m1$) and radioresistive ($m2$) populations, and $D0_{T1}, D0_{T2}$ represent the T-cell $D0$ values for the radiosensitive ($T1$) and radioresistive ($T2$) populations. The extrapolation numbers $n1$ and $n2$ are defined as the ratio between the quasi-threshold dose Dq and $D0$ values such that $n1 = Dq_m/D0_{m2}$ and $n2 = Dq_m/D0_{m2}$. The coefficients on the front of each component represent the fraction of the radiosensitive and radioresistive subpopulations as obtained from literature [30, 31]. The three survival curves are plotted in Figure 2.4.1 for absorbed doses of 0-20 Gy. See the appendix for the parameter values and accompanying sources.

It is important to note that the biphasic curves represented by equations (2.4.2) and (2.4.3) are composite survival curves for two subpopulations with differing sensitivities. This format was inspired by a similar fit to the survival of anoxic and aerobic Chinese hamster cells in Fig 3.12 and equation (3.23) of Chadwick and Leenhouts 2012 [32].

In our initial conditions, we assume a spatiotemporal equilibrium for

$$\mathbf{u}_0 = [SF_{E0}(E_{0eq}), E_{0ss} - SF_{E0}(E_{0eq}), C_{eq}, P_{eq}, SF_m(m_{eq}), M_{eq}, \eta_{eq}, SF_T(T_{eq}), N_{eq}]^T,$$

where each relevant species is adjusted by survival fraction and E_{0ss} is the baseline concentration of endothelial cells. As assumed in the preceding work, $T_{eq} = \eta_{eq} =$

$M_{eq} = P_{eq} \approx 0$. Although the equilibrium concentration of T-cells was assumed to be zero, we included the survival fraction from equation (2.4.3) for later use with fractionated doses.

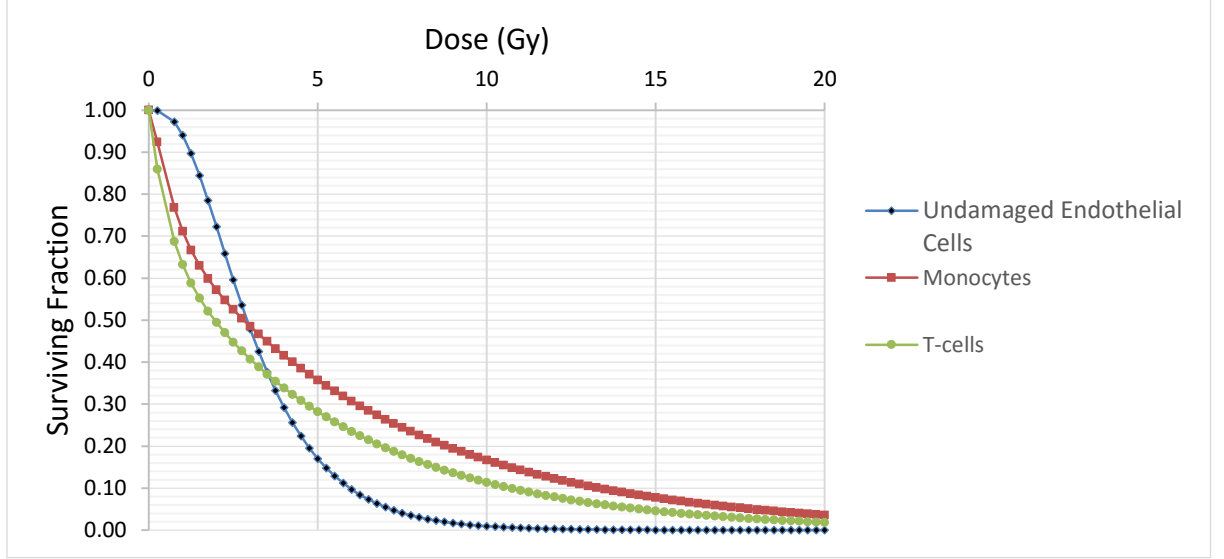


Figure 2.4.1. The surviving fraction of undamaged endothelial cells, monocytes, and T-cells after a single dose of ionizing radiation.

2.5 Boundary Conditions

Letting $\partial\Omega_L$ represent the boundary between the lumen and intima and $\partial\Omega_I$ represent the boundary between the intima and media [1], for the vector of species $\mathbf{v} = [C, P, M, \eta, N]^T$

it is assumed that there is zero flux across both boundaries such that $\frac{\partial \mathbf{v}}{\partial \mathbf{n}}|_{\partial\Omega_I \cup \partial\Omega_L} = 0$

(where \mathbf{n} is the outward unit normal vector).

The influx of monocytes and T-cells into the intima is assumed to be dependent on threshold levels of chemoattractant (C_{Tm} and C_{TT}), as similarly modeled by Ibragimov *et al.* [14]. For chemoattractant concentration equal to or below threshold value ($C \leq C_{Tm}$

and $C \leq C_{TT}$), the monocytes and T-cells are unable to cross the barrier between the lumen and intima. However, when this threshold concentration is surpassed ($C > C_{Tm}$ and $C > C_{TT}$), there is an immediate influx of white cells across $\partial\Omega_L$. Little *et al.* [1] derived volumetric source terms for each species from data in Takaku *et al.* and Klouche *et al.* [33, 34] in units of mol/m³s:

$$f_m(C, m_L)|_{\partial\Omega_L} = \begin{cases} D_m m_L (\beta_{m,0} + \beta_{m,1} C), & C > C_{Tm} \\ 0, & \text{otherwise} \end{cases} \quad (2.5.1)$$

$$f_T(C, T_L)|_{\partial\Omega_L} = \begin{cases} D_T T_L (\beta_{T,0} + \beta_{T,1} C), & C > C_{TT} \\ 0, & \text{otherwise} \end{cases} \quad (2.5.2)$$

where D_m and D_T are the diffusion rates of monocytes and T-cells, m_L and T_L are the average luminal concentrations, and $\beta_{m,0}, \beta_{m,1}, \beta_{T,0}, \beta_{T,1}$ are best-fit parameters from least-squares fitting [1]. We assumed zero flux across $\partial\Omega_I$ for monocytes and T-cells. To avoid convergence problems, we used the built-in, smoothed Heaviside function `flsmhs(x, scale)` available in COMSOL [2] for $x = C - C_{Tm}$ or $x = C - C_{TT}$ and $\text{scale} = 1E-20$. This function takes on the value 0 for $x < -\text{scale}$ and the value 1 for $x > \text{scale}$.

2.6 Time-Dependent Solver

COMSOL Multiphysics [2] offers a large selection of direct and iterative solvers. After performing a mesh refinement study, we opted for a physics-controlled mesh (mesh adapted to the geometry of the model) with a normal element size. We selected a relative tolerance of 1E-7 and an absolute tolerance of 5E-4 to ensure a smooth solution. Since our system of equations was strongly coupled, a direct solver was the best approach to guarantee convergence.

CHAPTER 3

RESULTS

3.1 Time Scale and Absorbed Dose

We ran our model for two separate time durations (90 seconds and 6 hours) for varied doses of acutely delivered radiation at $t = 0$ seconds. We chose a standard dose interval of 0 – 5 Gy, which is representative of a single dose (out of multiple fractions) of curative or adjuvant radiation therapy, but does not account for the mean dose received by the large arteries (which would be less depending on field arrangement). For example, a patient suffering from breast cancer may receive a standard whole breast dose of 45-50 Gy over 5-5.5 weeks (1.8-2.0 Gy/fraction per day) or 42.5 Gy in 16 fractions delivered in just over 3 weeks (2.66 Gy/fraction per day) [35]. In rare instances of metastatic breast cancer with bone metastases to the vertebral column, a patient seeking palliative treatment may receive a single fraction of radiotherapy as high as 8 Gy [36, 37]; however, due to computational limitations we chose not to examine doses exceeding 5 Gy.

3.2 Graphical Results

In Figure 3.2.1, we plot the concentration of monocytes and T-cells as a function of time after exposure (see the appendix for corresponding convergence plots). For doses below 2.2 Gy, it is obvious that the chemoattractant threshold (discussed in section 2.5) is not surpassed, as there is no evidence of monocyte or T-lymphocyte flux into the intima. The intimal concentration of T-cells does not increase with time ($T_{eq} = T_{final} = 0$), and the monocyte concentration is unchanged after initial perturbation due to radiation-induced

death. However, when a dose of approximately 2.2 Gy is met or exceeded, the risk of atherosclerosis increases considerably. At this point, there is a marked burst in chemoattractant concentration over the threshold value and subsequent influx of immune cells (monocytes and T-cells) into the intima. This, in turn, increases the concentration of proliferation factor (M-CSF), which induces differentiation of monocytes into macrophages. The increased number of macrophages are able to bind lipid (η) and thus contribute to the growth of the necrotic core, a key component in induction of cardiovascular disease.

In Figure 3.2.2 A and B, the concentration of undamaged endothelial cells increases slowly with time as the cells repopulate after initial damage. The concentration of damaged endothelial cells (Figure 3.2.2 C and D) is unchanged as we did not incorporate cellular repair processes into our model, but rather assumed that the proliferation of endothelial cells is dependent on the difference between baseline concentration and concentration of undamaged cells ($E_{0ss} - E_0$). In Figure 3.2.2. E and F, the concentration of chemoattractant MCP-1 increases rapidly for absorbed doses at or above 2.0 Gy and decreases for sub-threshold doses. For doses of 3.0-5.0 Gy, the concentration of MCP-1 appears to follow a log-normal distribution; however, the tail of the distribution flattens linearly at threshold concentration ($2.16E-8$ mol/m³). The concentration evolution of intimal MCP-1 at four different time points (0, 180, 1800, and 5400 s) can be seen in the volume plots in Figure 3.2.3.

In Figure 3.2.2, the proliferation factor (G, H), macrophage (K, L), macrophage-bound lipid (M, N), and necrotic core (Q, R) concentrations, which are all strongly-coupled,

initially grow at an exponential rate and then increase as linear functions of time after exposure. Of note, the graphs of proliferation factor and necrotic core concentration after irradiation with 3.0 and 4.0 Gy are overlapping (the yellow obscures the pink curve in the left panel); however, we can see that the graphs eventually diverge (right panel). Eventually, the combined monocyte (I, J), macrophage (K, L), and T-cell (O, P) concentrations are sufficient to cause degradation of chemoattractant (MCP-1) (via the last three terms in row three of equation (2.3.3)) at approximately 0.05 hour, and between 0.5-1.5 hours (depending on administered dose) after exposure, the MCP-1 concentration decays to threshold value, preventing further influx of monocytes and T-cells. It is important to note that although the T-cell concentration appears to asymptote at 0.5, 1.0, and 1.5 hours (3.0, 4.0, and 5.0 Gy), after a sufficiently long enough period the concentration begins to slowly decay to its equilibrium value. The proliferation factor, which depends exclusively on T-cell concentration, is predicted to follow a similar decay pattern (results not obtained due to computational limitations), and eventually the concentrations of macrophages (M) and macrophage-bound lipid (η) should also return to equilibrium levels.

The brief perturbation of endothelial cells and monocytes in Figure 3.2.2 are dependent on their survival curves, which are modeled as shouldered exponential functions of dose. Due to the broad shoulder for undamaged endothelial cells (EC's), the survival of this cell type is relatively unchanged for the first 0.5 Gy, but then decreases rapidly until 3.0 - 4.0 Gy, at which point the rate of change begins to asymptote. This trend is reflected in Figure 3.2.2 (A-D), as the damaged EC concentration is a function of the undamaged EC concentration ($E_1 = E_{0ss} - E_0$, for E_{0ss} the baseline EC concentration).

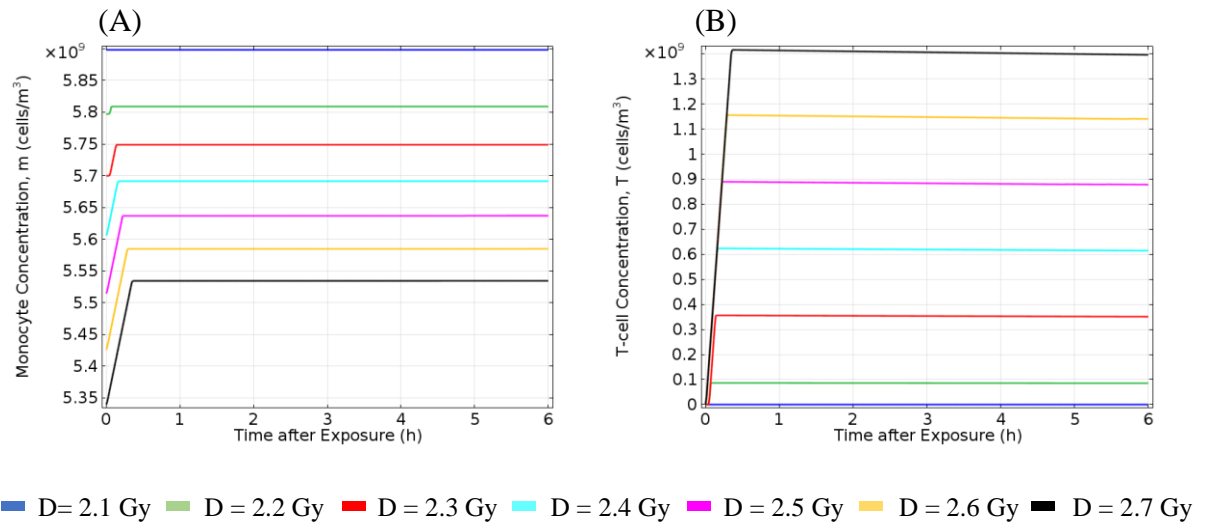
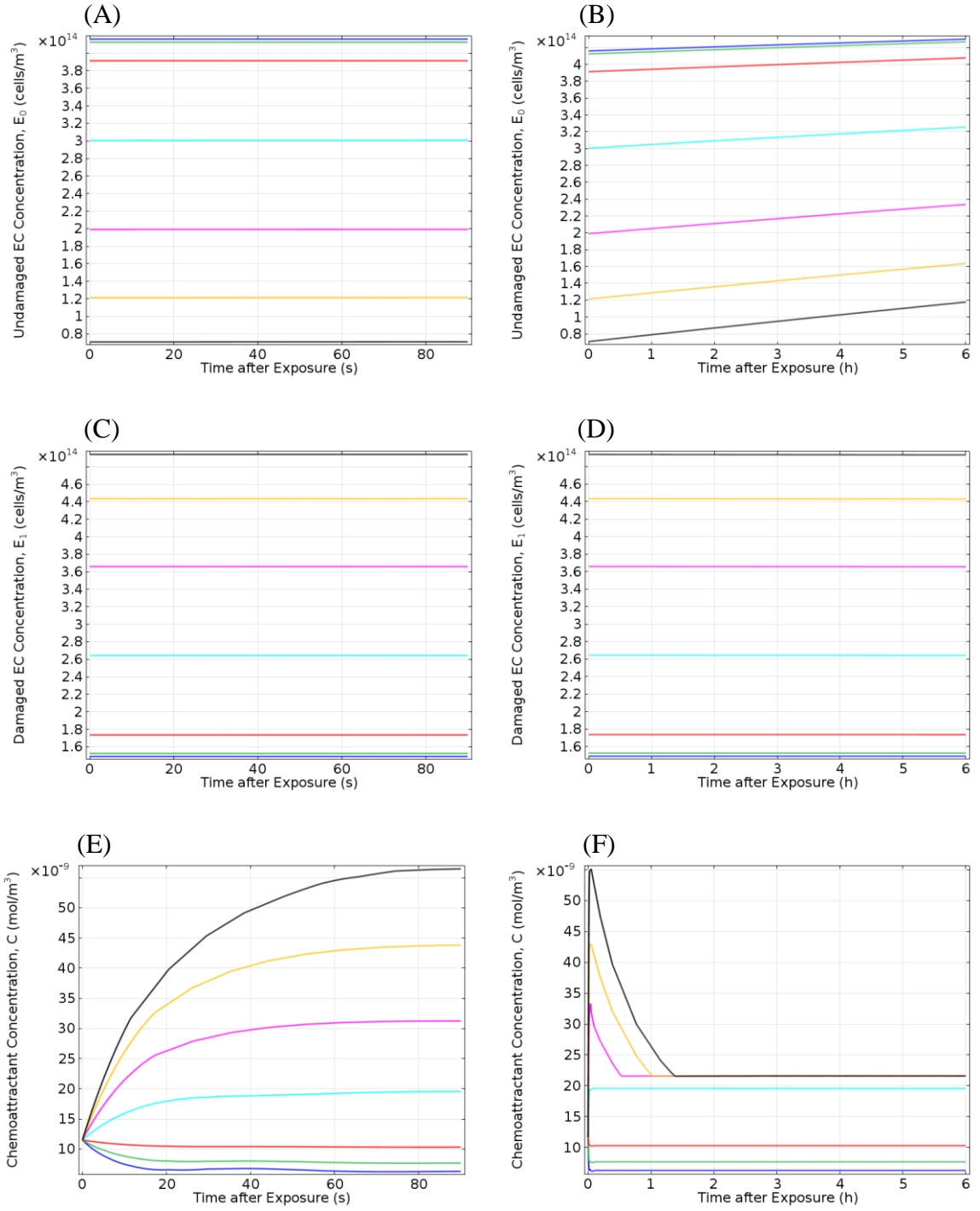
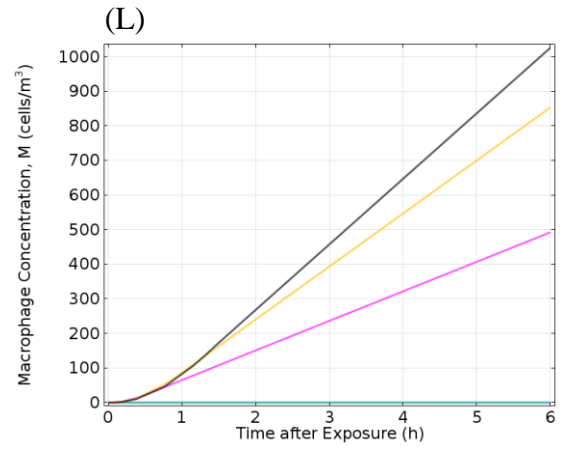
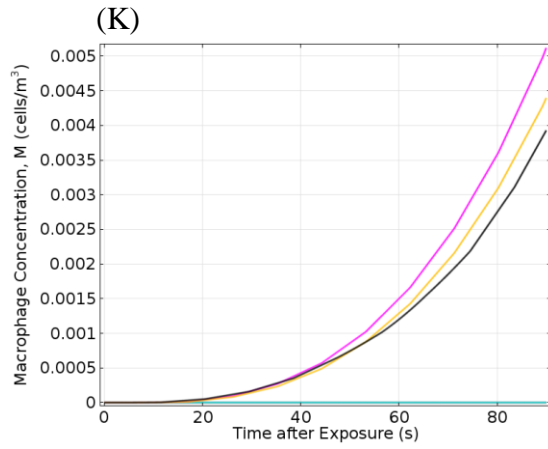
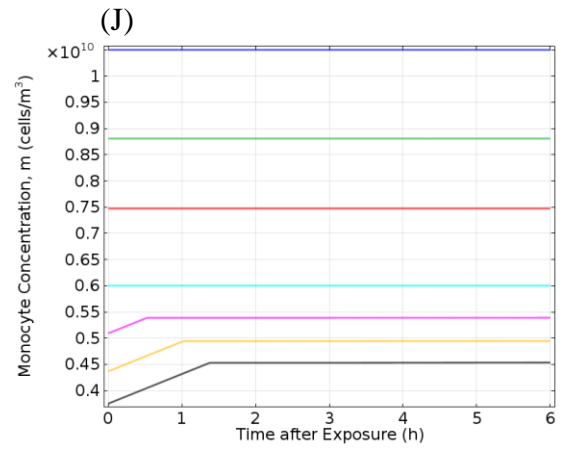
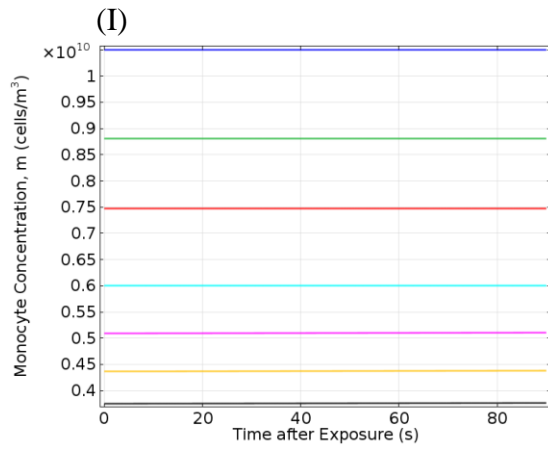
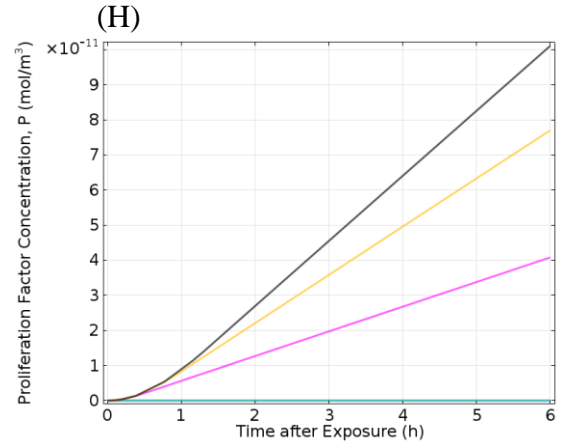
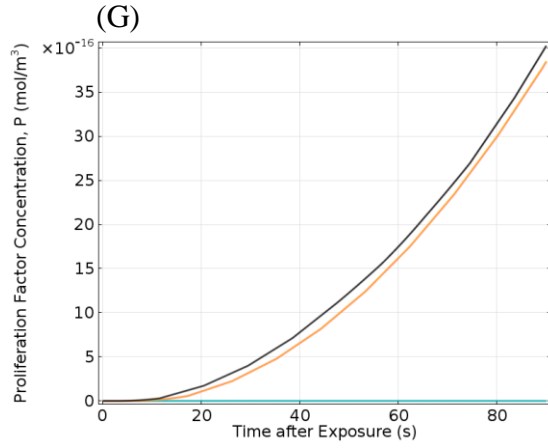


Figure 3.2.1. Monocyte (A) and T-cell (B) response to varied doses (2.1-2.7 Gy) of ionizing radiation (administered at $t = 0$ h). As can be visualized by the abrupt increase in intimal immune cells, the chemoattractant threshold is surpassed at approximately 2.2 Gy.



■ $D = 2.1$ Gy
 ■ $D = 2.2$ Gy
 ■ $D = 2.3$ Gy
 ■ $D = 2.4$ Gy
 ■ $D = 2.5$ Gy
 ■ $D = 2.6$ Gy
 ■ $D = 2.7$ Gy



■ D = 2.1 Gy
 ■ D = 2.2 Gy
 ■ D = 2.3 Gy
 ■ D = 2.4 Gy
 ■ D = 2.5 Gy
 ■ D = 2.6 Gy
 ■ D = 2.7 Gy

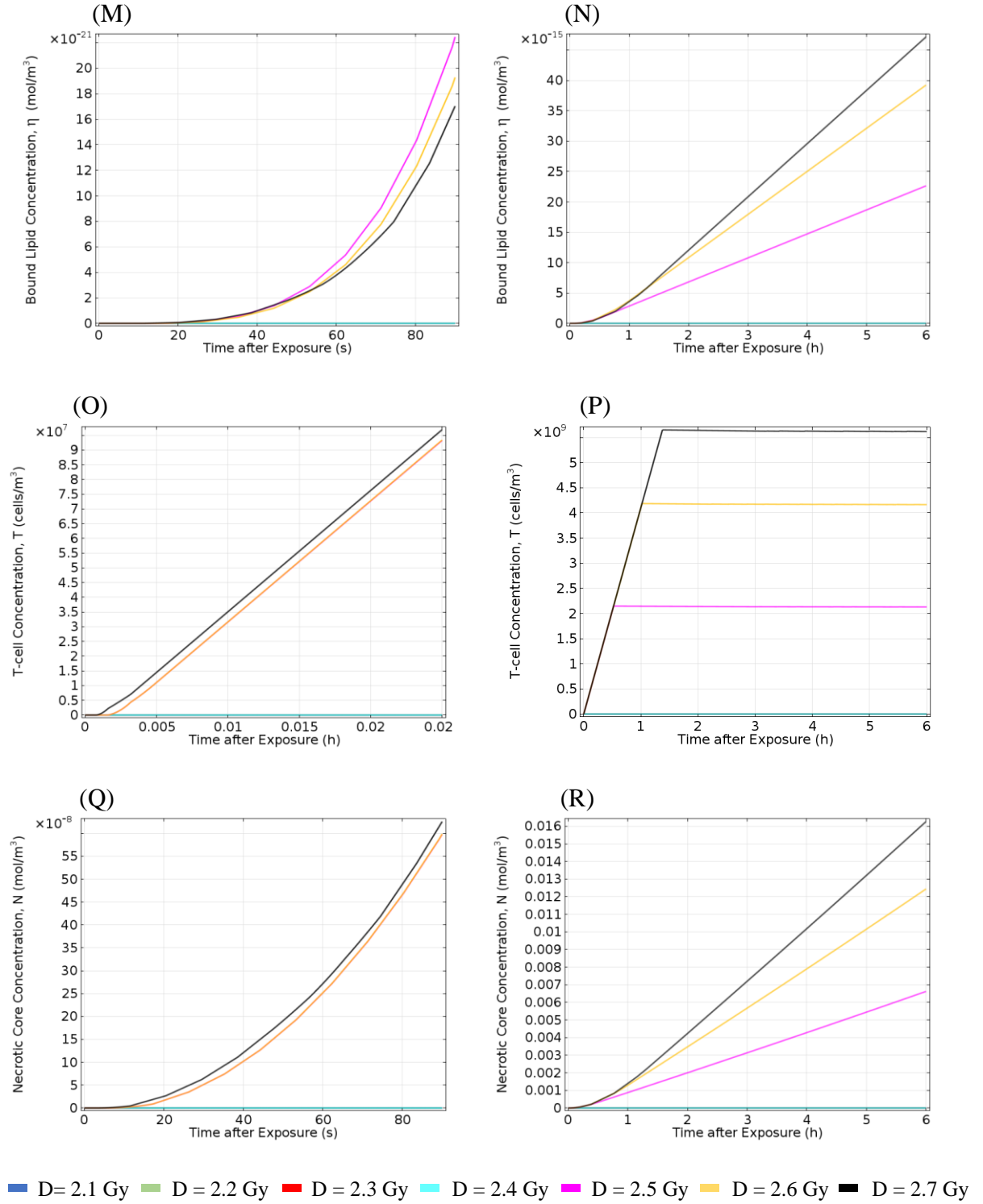


Figure 3.2.2 The effect of single doses of ionizing radiation (administered at $t = 0$ h) on the concentrations of nine species involved in atheroma development 0 – 90 seconds (left panel) and 0 – 6 hours (right panel) post-radiation. (A, B) Undamaged and (C, D) damaged endothelial cell concentrations as a function of time after exposure. (E, F) Chemoattractant (MCP-1), (G, H) proliferation factor (M-CSF), (I, J) monocyte, (K, L) macrophage, (M, N) macrophage-bound lipid, (O, P) T-cell, and (Q, R) necrotic core cocentrations as a function of time after exposure.

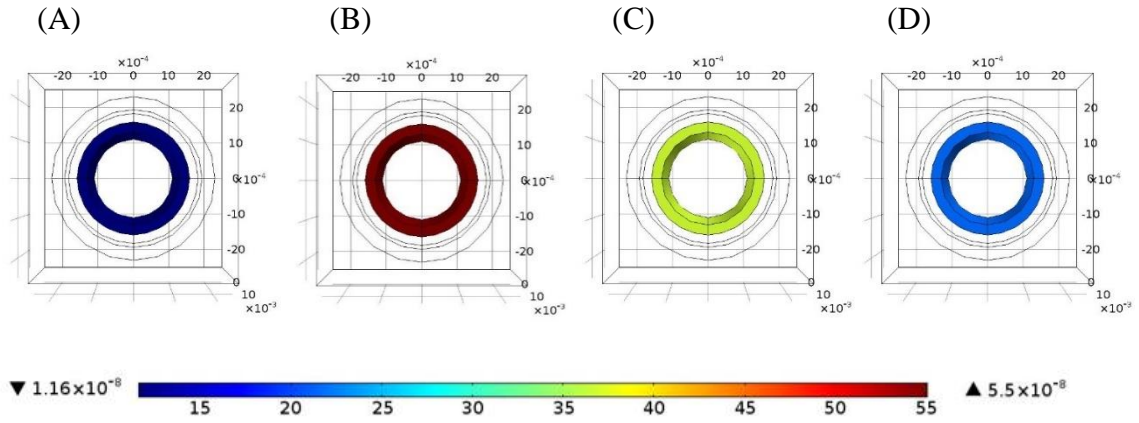


Figure 3.2.3 Intima cross sections at four different time points (A) 0 s (B) 180 s (C) 1800 s (D) 5400 s. The concentration of MCP-1 (color-coded) after 5 Gy rapidly reaches peak value within 180 s and then slowly decays to threshold (2.16×10^{-8} mol/m³) at 5400 seconds (1.5 hour).

CHAPTER 4

DISCUSSION

4.1 Findings and Limitations

We have extended the results of the Little *et al.* 2009 study [1] of early-stage atherosclerosis using numerical methods, with particular attention to survival fraction after irradiation. In our analyses, we utilized an incredibly powerful software package, COMSOL Multiphysics, to handle a large system of nine strongly-coupled partial differential equations. We constructed a three-layered, three-dimensional annular prism to model the geometry of the human coronary artery and defined our system within the intima domain.

Our results of MCP-1 variation for doses at or below 1.0 Gy (Figure 3.2.2 E) suggest that the concentration of chemoattractant decreases before leveling off; whereas, Little *et al.* [1] discovered an upward trend in MCP-1 for small doses of 10 mGy (Figure 5 [1]). The discrepancies between our results and those found by Little *et al.* [1] are likely due to the assumed hypothesis of cell survival. Little *et al.* [1] adopted a single-target single-hit hypothesis, which assumes that cell survival is a linear function of absorbed dose. This model is appropriate for low doses of exposure, such as those received in occupational settings. However, our research focused on higher doses at the therapeutic level, which are more appropriately modeled under the multi-target single-hit hypothesis. Our model could be easily adjusted to incorporate both survival hypotheses, an endeavor that we plan to carry out in future analyses.

There are several limitations of this model that require further acknowledgement. First, we used a rather simplified system of equations that incorporated the major components of the early-stage processes, excluding other contributors such as high-density lipoprotein (HDL), radicals, and antioxidants present in the lumen. These simplifications were necessary in order to be able to solve the system with our available computing resources. In addition, we modeled concentration changes after a single dose, rather than multiple fractionated doses - which is more consistent with radiotherapy routines. Unfortunately, in order to effectively model fractionation effects, the doses would have to be administered at different time points, which adds another level of complexity to our system. In order to allow sufficient recovery time between doses (generally a one-day hiatus), we would have to run our simulation for 16-24 times the current study period (4-6 fractions) and have enough available disk space to store the temporary solutions. Although it is certainly possible, it is not necessarily feasible with our current computing capabilities.

4.2 Radiological Implications

Radio-therapeutic treatment of certain cancers located within proximity to large arteries (such as the cerebral, carotid, or coronary arteries) increases the risk of death from cardiovascular disease. The Surveillance, Epidemiology, and End Results (SEER) program of the National Cancer Institute conducted a longitudinal cohort study of 308,861 women treated for breast cancer between the years 1973 to 2001, of whom 115,165 (37%) received radiotherapy as part of their treatment strategy. Of the patients diagnosed between the years 1973-82, the cardiac mortality ratio of left versus right-sided cancer (95% CI) was 1.58

(1.2-1.95), 15 plus years after radiation [38]. Although doses administered in the 1970-80's were considerably more generous than contemporary techniques, these striking differences in cardiac deaths due to beam placement highlight the importance of further cardiovascular protection measures. Total body irradiation (TBI) prior to stem cell transplant or due to radiological incidents (e.g. nuclear facility breach or terrorism) can involve adverse cardiovascular effects [39, 40], as well as radiation to other cancer types such as brain and spinal tumors or lung cancer [41-43].

Our methods differ from Little *et al.* [1] in several ways. First, we solved the system of reaction-diffusion equations numerically (rather than analytically, as was done in the previous study). Numerical methods enable us to solve more sophisticated and spatially heterogeneous conditions, though in the current study we have not taken advantage of analyzing spatial heterogeneity. We also incorporated cell survival curves within the initial conditions, considering the differing radiosensitivities of the monocyte and T-cell subpopulations as well as the shoulder width of each survival curve. This enabled us to examine doses within therapeutic range (≥ 1.8 Gy), which would not have been appropriate using the earlier model. Unlike the previous study, we used the volumetric source terms given in equations (2.5.1) and (2.5.2) within our boundary conditions, rather than converting to a change in concentration per unit distance as was done in Little *et al.* [1]. Finally, we updated the table of parameter values to include more current values where possible, the physical properties of the artery, and constants specific to the survival curves.

We have shown that there is an increase in atheroma size, and thus increased risk of an adverse cardiac event, associated with absorbed radiation doses of greater than or equal

to 2.2 Gy, assuming that there exist MCP-1 thresholds for monocyte and T-cell flux. These results have tremendous implications on current radiotherapy routines, which typically employ daily conventional or hypo-fractionated doses of at least 1.8-2.0 Gy, but can deliver upwards of 2.0 Gy for certain regimens. Investigators and medical professionals with access to the COMSOL software can easily modify the administered dose or time after exposure within the study section of the model builder under the “time dependent” tab. We expect that these numerical results can be used in conjunction with *in vivo* or *in vitro* studies to better understand the post-radiation pro-inflammatory process involved in the development of cardiovascular disease.

APPENDIX
TABLE OF PARAMETERS

Name	Expression	Description	Source
τ	4.63E-06[1/s]	Endothelial cell repopulation rate	Little et al. 2009 (Table S2) [1]
E_{0ss}	5.65E+08[cells/ml]	Baseline endothelial cell concentration	Derived from Hillebrand et al. 2007 (pg 643) [44]
ι_{LO}	6.14E+01[ml/(mol*s)]	Endothelial cell damage rate per unit concentration of fully-oxidized LDL	Little et al. 2009 (Table S2) [1]
d_E	5.29E-08[1/s]	Damaged endothelial cell death/degradation rate	Little et al. 2009 (Derived via Eq. 20) [1]
ρ_{CE}	5.73E-24[mol/(cell*s)]	Production rates of MCP-1 per unit concentration of damaged endothelial cells	Little et al. 2009 (Table S2) [1]
ρ_{CM}	1.96E-25[mol/(cell*s)]	Production rates of MCP-1 per unit concentration of macrophages	Little et al. 2009 (Table S2) [1]
ρ_{CT}	0.00E+00[mol/(cell*s)]	Production rates of MCP-1 per unit concentration of T-cells	Little et al. 2009 (Table S2) [1]
D_C	3.89E-11[m^2/s]	MCP-1 diffusion rate	Little et al. 2009 (Table S2) [1]
d_{CM}	1.29E-05[ml/(cell*s)]	Degradation rate of MCP-1 per unit concentration of macrophages	Little et al. 2009 (Table S2) [1]
d_{CT}	1.29E-05[ml/(cell*s)]	Degradation rate of MCP-1 per unit concentration of T-cells	Little et al. 2009 (Table S2) [1]
d_{cm}	1.29E-05[ml/(cell*s)]	Degradation rate of MCP-1 per unit concentration of monocytes	Little et al. 2009 (Table S2) [1]
ρ_{PT}	9.15E-25[mol/(cell*s)]	Production rate of M-CSF per unit concentration of T-cells	Little et al. 2009 (Table S2) [1]
D_P	1.82E-11[m^2/s]	M-CSF diffusion rate	Little et al. 2009 (Table S2) [1]
χ_m	3.00E+00[m^2*ml/(mol*s)]	Monocyte chemotactic factor	Little et al. 2009 (Table S2) [1]
χ_M	3.00E+00[m^2*ml/(mol*s)]	Macrophage chemotactic factor	Little et al. 2009 (Table S2) [1]
χ_T	3.00E+00[m^2*ml/(mol*s)]	T-cell chemotactic factor	Little et al. 2009 (Table S2) [1]
ρ_{mP}	1.39E+07[ml/(mol*s)]	Proliferation rate of monocytes per unit concentration of proliferation factor	Derived from Becker et al. 1987 (Figure 1) and Knowles 2001 [45, 46]
ρ_M	8.00E+06[ml/(mol*s)]	Conversion rate of monocytes to macrophages	Derived from Becker et al. 1987 (Figure 1) and Knowles 2001 [45, 46]
D_m	3.03E-15[m^2/s]	Monocyte diffusion rate	Little et al. 2009 (Table S2) [1]
D_M	2.87E-15[m^2/s]	Macrophage diffusion rate	Little et al. 2009 (Table S2) [1]
L_0	3.08E-10[mol/ml]	Concentration of oxidized LDL within the intima	Geometric mean of Napoli et al. 1997 & Bing et al. 2004 [47, 48]
d_T	6.94E-07[1/s]	T-cell degradation rate	Little et al. 2009 (Table S2) [1]
D_T	6.21E-15[m^2/s]	T-cell diffusion rate	Little et al. 2009 (Table S2) [1]

d_{MM}	1.50E-08[mol/cell]	Ratio of the augmentation of necrotic core by macrophage death	Little et al. 2009 (Table S2) [1]
d_{TT}	2.05E-10[mol/cell]	Ratio of the augmentation of necrotic core by T-cell death	Little et al. 2009 (Table S2) [1]
m_L	3.00E+05[cells/ml]	Concentration of monocytes within the lumen	Little et al. 2009 (Table S2) [1]
β_{m0}	1.72E+08[1/m^2]	Best fit parameter in function $f_m(C, m_L)$	Little et al. 2009 (Table S2) [1]
β_{m1}	2.53E+19[ml/(mol*m^2)]	Best fit parameter in function $f_m(C, m_L)$	Little et al. 2009 (Table S2) [1]
C_{Tm}	2.16E-14[mol/ml]	Threshold concentration of MCP-1 required for monocyte flux into intima	Derived from Gonzalez-Quesada et al. 2009 and ThermoFisher Scientific [49, 50] ^a
T_L	2.50E+06[cells/ml]	T-cell concentration within the lumen	Little et al. 2009 (Table S2) [1]
β_{T0}	7.33E+07[1/m^2]	Best fit parameter in function $f_T(C, T_L)$	Little et al. 2009 (Table S2) [1]
β_{T1}	8.85E+18[ml/(mol*m^2)]	Best fit parameter in function $f_T(C, T_L)$	Little et al. 2009 (Table S2) [1]
C_{TT}	2.16E-14[mol/ml]	Threshold concentration of MCP-1 required for T-cell flux into intima	Approximated equal to C_{Tm}
C_{eq}	1.15E-14[mol/ml]	Equilibrium concentration of MCP-1 within the intima	Little et al. 2009 (Table S2) [1]
m_{eq}	1.05E+04[cells/ml]	Equilibrium concentration of monocytes within the intima	Derived from Joris et al. 1979 and ScienCell [51, 52] ^b
E_{0eq}	4.48E+08[cells/ml]	Equilibrium concentration of endothelial cells	Derived from Hillebrand et al. 2007, Harvey et al. 2010, He et al. 2000, Staiger et al. 2004 [44, 53-55] ^c
E_{1eq}	1.17E+08[cells/ml]	Equilibrium concentration of damaged endothelial cells	$E_{0ss} - E_{0eq}$
N_{eq}	0.00E+00[mol/ml]	Equilibrium concentration of the necrotic core	Assumed prior to plaque formation
P_{eq}	0.00E+00[mol/ml]	Equilibrium concentration of M-CSF within the intima	Little et al. 2009 (Table S2) [1]
M_{eq}	0.00E+00[cells/mm^3]	Equilibrium concentration of macrophages within the intima	Little et al. 2009 (Table S2) [1]
η_{eq}	0.00E+00[mol/ml]	Equilibrium concentration of macrophage-bound lipid within the intima	Little et al. 2009 (Table S2) [1]
T_{eq}	0.00E+00[cells/mm^3]	Equilibrium concentration of T-cells within the intima	Little et al. 2009 (Table S2) [1]
R_2	7.66E+13[cell/(mol*s)]	Derived scaling constant in function $d_M(\eta/M)$	Little et al. 2009 (Table S2) [1]
E	1.48E+06[Pa]	Young's modulus for coronary artery tissue	Karimi et al. 2013 [56]
ν	4.95E-01	Poisson's ratio for coronary artery tissue	Karimi et al. 2013 [56]
ρ_a	1.07E+00[g/ml]	Density of arterial wall (canine)	Armentano et al. 1995 [57]
T_{LAD}	1.10E+00[mm]	Anterior/Posterior wall thickness of LAD	Perry et al. 2013 [58]
D_{LAD}	2.20E+00[mm]	Luminal diameter of the LAD	Perry et al. 2013 [58]
h_{LAD}	1.50E-02[m]	Height of LAD	User Chosen
T_{EAT}	5.00E+00[mm]	Epicardial adipose tissue thickness	Bertaso et al. 2013 [59] ^d
ρ_{EAT}	1.55E+00[g/cm^3]	Density of epicardial adipose tissue	Derived from Marcus et al. 2007, Duchesne et al. 2009 [60, 61] ^e
ρ_b	1.05E+03[kg/m^3]	Density of blood	Hinghofer-Szalkay et al. 1987 (Fig. 1) [62] ^f

μ_b	3.63E+00[cP]	Dynamic viscosity of blood at 37°C	Chandler et al. 1986 [63]
v_{LAD}	2.70E+01[cm/s]	Resting average peak blood velocity in the LAD	Anderson et al. 2000 (Table 3.) [64]
p_{LAD}	9.05E+01[mmHg]	Diastolic Pressure in the LAD	Dole et al. 1984 (TABLE) [65] ^a
IT	2.35E-01[mm]	Intimal thickness of the human coronary artery	Mukherjee et al. 2010 (pg 356) [66]
MT	2.00E-01[mm]	Media thickness of the human coronary artery	Mukherjee et al. 2010 (pg 356) [66]
AT	4.00E-01[mm]	Aventitia thickness of the human coronary artery	Mukherjee et al. 2010 (pg 356) [66]
$\rho_{in,0}$	5.34E-10[ml/(cell*s)]	Macrophage ingestion rate of oxidized LDL at zero concentration of bound lipid	Little et al. 2009 (Table S2) [1]
$\rho_{in,high}$	2.67E-10[ml/(cell*s)]	Macrophage ingestion rate of oxidized LDL at high concentration of bound lipid	Little et al. 2009 (Table S2) [1]
R_3	2.09E+02[cell/mol]	Derived scaling constant in function $\rho_{in}(\eta/M)$	Little et al. 2009 (Table S2) [1]
d_{M0}	9.26E-07[1/s]	Macrophage death rate	Little et al. 2009 (Table S2) [1]
ϕ_{m1}	2.50E-01	Percent radiosensitive monocytes	Kwan and Norman 1978 [31]
ϕ_{m2}	7.50E-01	Percent radioresisitive monocytes	Kwan and Norman 1978 [31]
$D0_{m1}$	5.50E-01[Gy]	The required dose necessary to kill 63% of the radiosensitive monocyte population	Kwan and Norman 1978 [31]
$D0_{m2}$	6.50E+00[Gy]	The required dose necessary to kill 63% of the radioresistive monocyte population	Kwan and Norman 1978 [31]
Dq_m	2.50E-01[Gy]	The quasi-threshold dose for the monocyte population	Estimated from data in Fig 1. of Kwan and Norman 1978 [31]
n_1	1.58E+00	Defined as $\exp\left(\frac{Dq_m}{D0_{m1}}\right)$	Derived using equations in Chapter 2 of Beyzadeoglu et al. 2010 [25]
n_2	1.04E+00	Defined as $\exp\left(\frac{Dq_m}{D0_{m2}}\right)$	Derived using equations in Chapter 2 of Beyzadeoglu et al. 2010 [25]
ϕ_{T1}	3.00E-01	Percent radiosensitive T-cells	Kwan and Norman 1977 [30]
ϕ_{T2}	7.00E-01	Percent radioresisitive T-cells	Kwan and Norman 1977 [30]
$D0_{T1}$	5.50E-01[Gy]	The required dose necessary to kill 63% of the radiosensitive T-cell population	Kwan and Norman 1977 [30]
$D0_{T2}$	5.50E+00[Gy]	The required dose necessary to kill 63% of the radioresistive T-cell population	Kwan and Norman 1977 [30]
$D0_{E0}$	1.69E+00[Gy]	The required dose necessary to kill 63% of the undamaged endothelial cell population	Park et al. 2012 [29]
Dq_{E0}	2.12E+00[Gy]	The quasi-threshold dose for the undamaged endothelial cell population	Park et al. 2012 [29]
n	3.51E+00	Defined as $\exp\left(\frac{Dq_{E0}}{D0_{E0}}\right)$	Derived using equations in Chapter 2 of Beyzadeoglu et al. 2010 [25]

^aUsed molecular weight of 11 kDa [50] to convert from 238 pg/ml [49] to 2.16E-14 mol/ml.

^bAverage number of intimal monocytes, 2.1 monocytes/100 endothelial cells [51] multiplied by the average volume of human coronary artery endothelial cells 5E5 endothelial cells/ml [52].

^cEquilibrium concentration of endothelial cells (undamaged+damaged) [44] multiplied by the arithmetic mean of equilibrium percentages of undamaged endothelial cells [53-55].

^dAs defined by Bertaso *et al.* [59], a tissue thickness of 5 mm should represent a healthy cutoff for low-risk populations

^eEpicardial adipose tissue has an attenuation value of -65 Hounsfield units (HU) [61]. We converted to a density of 1.55 g·cm⁻³ using a method described in Duchesne *et al.* [60] and the density of water as a reference value.

^fArithmetic mean of max and min venous blood densities of 6 male subjects in sitting, standing, and supine position from Fig. 1 of Hinghofer-Szalkay *et al.* [62].

^gAverage of the initial and final mean diastolic pressures given in Dole *et al.* [65].

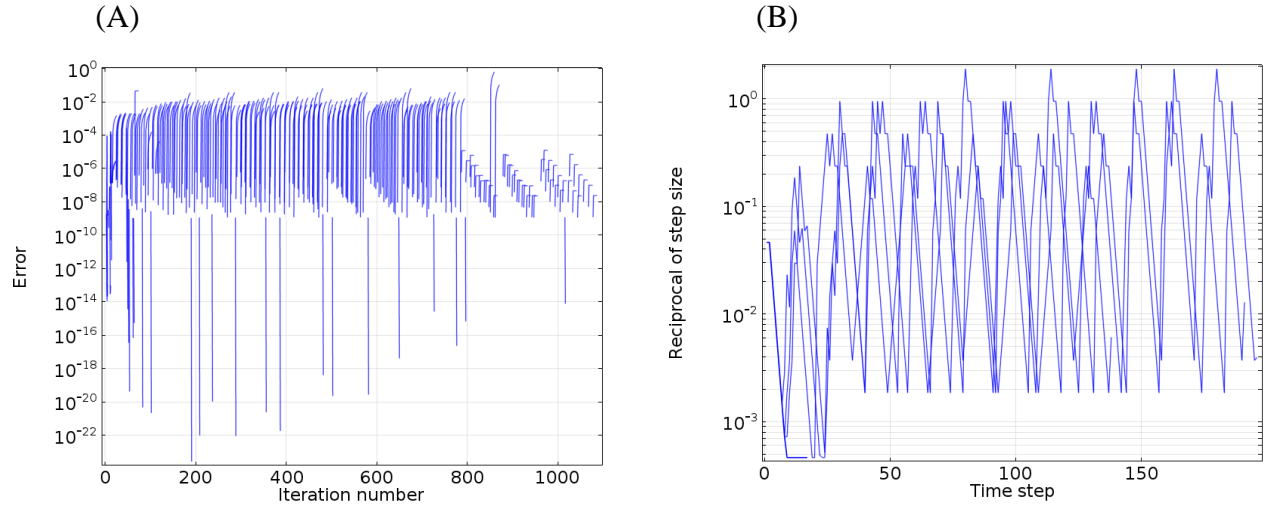


Figure A.1 (A) Estimate of relative error at each iteration for a convergence criterion of 1E-7. (B) Convergence of the time-dependent solver for varied absorbed doses.

In Figure A.1 (A), the error estimates are graphed at each iteration of the segregated solver (direct solver for the coupled system and iterative solver for the laminar flow module). The first 800 iterations represent the error estimates for the direct solver across seven dose parameters (0 - 5 Gy). Figure A.1 (B) is a plot of the reciprocal of step size versus time step in the time-dependent solver for each of the seven dose parameters. As the absorbed dose increases, convergence becomes more difficult to achieve.

BIBLIOGRAPHY

1. Little, M.P., A. Gola, and I. Tzoulaki, *A Model of Cardiovascular Disease Giving a Plausible Mechanism for the Effect of Fractionated Low-Dose Ionizing Radiation Exposure*. PLoS Computational Biology, 2009. **5**(10): p. e1000539.
2. COMSOL Multiphysics v. 4.4. COMSOL AB, Stockholm, Sweden.
3. Prasad, D.S., et al., *Subclinical atherosclerosis and silent myocardial ischaemia in patients with type 2 diabetes: a protocol of a clinico-observational study*. Open Heart, 2014. **1**(1): p. e000100.
4. Hansson, G.K., *Inflammation, atherosclerosis, and coronary artery disease*. N Engl J Med, 2005. **352**(16): p. 1685-95.
5. Krause, W.J., *The Art of Examining and Interpreting Histologic Preparations: A Laboratory Manual and Study Guide for Histology*. 2004: Universal Publishers.
6. Lusis, A.J., *Atherosclerosis*. Nature, 2000. **407**(6801): p. 233-41.
7. Minamino, T., et al., *Endothelial cell senescence in human atherosclerosis: role of telomere in endothelial dysfunction*. Circulation, 2002. **105**(13): p. 1541-4.
8. Lomax, M.E., L.K. Folkes, and P. O'Neill, *Biological consequences of radiation-induced DNA damage: relevance to radiotherapy*. Clin Oncol (R Coll Radiol), 2013. **25**(10): p. 578-85.
9. Lam, J. *Atherosclerosis*. 2016]; Available from: <http://www.merckmanuals.com/home/heart-and-blood-vessel-disorders/atherosclerosis/atherosclerosis#>.
10. Xu, J. and Y. Cao, *Radiation-induced carotid artery stenosis: a comprehensive review of the literature*. Interv Neurol, 2014. **2**(4): p. 183-92.
11. Su, Y., et al., *Analysis of ionizing radiation-induced DNA damage and repair in three-dimensional human skin model system*. Exp Dermatol, 2010. **19**(8): p. e16-22.
12. Abraham, D. and O. Distler, *How does endothelial cell injury start? The role of endothelin in systemic sclerosis*. Arthritis Research & Therapy, 2007. **9**(Suppl 2): p. S2-S2.
13. Rice-Evans, C.A. and R.H. Burdon, *Free Radical Damage and its Control*. 1994: Elsevier Science.

14. Ibragimov, A.I., et al., *A mathematical model of atherogenesis as an inflammatory response*. Math Med Biol, 2005. **22**(4): p. 305-33.
15. Galkina, E. and K. Ley, *Immune and Inflammatory Mechanisms of Atherosclerosis*. Annual review of immunology, 2009. **27**: p. 165-197.
16. Hajjar, D.P. and M.E. Haberland, *Lipoprotein trafficking in vascular cells. Molecular Trojan horses and cellular saboteurs*. J Biol Chem, 1997. **272**(37): p. 22975-8.
17. Fok, P.W., *Growth of necrotic cores in atherosclerotic plaque*. Math Med Biol, 2012. **29**(4): p. 301-27.
18. Iles, R. and S. Docherty, *Biomedical Sciences: Essential Laboratory Medicine*. 2011: Wiley.
19. University of Minnesota. *Coronary Arteries*. Atlas of Human Cardiac Anatomy [cited 2016; Available from: <http://www.vhlab.umn.edu/atlas/coronary-arteries/>].
20. Baert, A.L., M. Oudkerk, and M.F. Reiser, *Coronary Radiology*. 2010: Springer Berlin Heidelberg.
21. Marín-García, J., *Post-Genomic Cardiology*. 2014: Elsevier Science.
22. Waller, B.F., et al., *Anatomy, histology, and pathology of coronary arteries: A review relevant to new interventional and imaging techniques—Part II*. Clinical Cardiology, 1992. **15**(7): p. 535-540.
23. Demircelik, M.B., et al., *Epicardial adipose tissue and pericoronary fat thickness measured with 64-multidetector computed tomography: potential predictors of the severity of coronary artery disease*. Clinics, 2014. **69**(6): p. 388-392.
24. Zhao, B., et al., *Constitutive receptor-independent low density lipoprotein uptake and cholesterol accumulation by macrophages differentiated from human monocytes with macrophage-colony-stimulating factor (M-CSF)*. J Biol Chem, 2006. **281**(23): p. 15757-62.
25. Beyzadeoglu, M., et al., *Basic radiation oncology*. 2010.
26. Nomiya, T., *Discussions on target theory: past and present*. Journal of Radiation Research, 2013. **54**(6): p. 1161-1163.
27. Abok, K., et al., *Macrophage radiosensitivity in culture as a function of exposure to ionic iron*. Virchows Arch B Cell Pathol Incl Mol Pathol, 1983. **42**(2): p. 119-29.

28. Lin, E.C., *Radiation Risk From Medical Imaging*. Mayo Clinic Proceedings, 2010. **85**(12): p. 1142-1146.
29. Park, M.-T., et al., *The radiosensitivity of endothelial cells isolated from human breast cancer and normal tissue in vitro*. Microvascular Research, 2012. **84**(2): p. 140-148.
30. Kwan, D.K. and A. Norman, *Radiosensitivity of Human Lymphocytes and Thymocytes*. Radiation Research, 1977. **69**(1): p. 143-151.
31. Kwan, D.K. and A. Norman, *Radiosensitivity of Large Human Monocytes*. 1978, Academic Press, Inc. p. 556.
32. Chadwick, K.H. and H.P. Leenhouts, *The Molecular Theory of Radiation Biology*. 2012: Springer Berlin Heidelberg.
33. Klouche, M., et al., *Enzymatically modified, nonoxidized LDL induces selective adhesion and transmigration of monocytes and T-lymphocytes through human endothelial cell monolayers*. Arterioscler Thromb Vasc Biol, 1999. **19**(3): p. 784-93.
34. Takaku, M., et al., *An in vitro coculture model of transmigrant monocytes and foam cell formation*. Arterioscler Thromb Vasc Biol, 1999. **19**(10): p. 2330-9.
35. Pierce, L., *Radiation therapy techniques for newly diagnosed, non-metastatic breast cancer*. . UpToDate, 2013.
36. Maranzano, E., et al., *8Gy single-dose radiotherapy is effective in metastatic spinal cord compression: results of a phase III randomized multicentre Italian trial*. Radiother Oncol, 2009. **93**(2): p. 174-9.
37. Souchon, R., et al., *DEGRO practice guidelines for palliative radiotherapy of metastatic breast cancer: bone metastases and metastatic spinal cord compression (MSSC)*. Strahlenther Onkol, 2009. **185**(7): p. 417-24.
38. Darby, S.C., et al., *Long-term mortality from heart disease and lung cancer after radiotherapy for early breast cancer: prospective cohort study of about 300,000 women in US SEER cancer registries*. Lancet Oncol, 2005. **6**(8): p. 557-65.
39. Baker, J.E., J.E. Moulder, and J.W. Hopewell, *Radiation as a risk factor for cardiovascular disease*. Antioxid Redox Signal, 2011. **15**(7): p. 1945-56.
40. Bhatia, S., *Long-term health impacts of hematopoietic stem cell transplantation inform recommendations for follow-up*. Expert review of hematology, 2011. **4**(4): p. 437-454.

41. Madan, R., et al., *Radiation induced heart disease: Pathogenesis, management and review literature*. Journal of the Egyptian National Cancer Institute, 2015. **27**(4): p. 187-193.
42. Plummer, C., et al., *Ischemic stroke and transient ischemic attack after head and neck radiotherapy: a review*. Stroke, 2011. **42**(9): p. 2410-8.
43. Yusuf, S.W., S. Sami, and I.N. Daher, *Radiation-induced heart disease: a clinical update*. Cardiol Res Pract, 2011. **2011**: p. 317659.
44. Hillebrand, U., et al., *Dose-dependent endothelial cell growth and stiffening by aldosterone: endothelial protection by eplerenone*. J Hypertens, 2007. **25**(3): p. 639-47.
45. Becker, S., M.K. Warren, and S. Haskill, *Colony-stimulating factor-induced monocyte survival and differentiation into macrophages in serum-free cultures*. J Immunol, 1987. **139**(11): p. 3703-9.
46. Knowles, D.M., *Neoplastic Hematopathology*. 2001: Lippincott Williams & Wilkins.
47. Bing, H., et al., *Positive correlation between in vivo oxidized LDL and LDL immune complexes*. Clin Biochem, 2004. **37**(1): p. 72-5.
48. Napoli, C., et al., *Fatty streak formation occurs in human fetal aortas and is greatly enhanced by maternal hypercholesterolemia. Intimal accumulation of low density lipoprotein and its oxidation precede monocyte recruitment into early atherosclerotic lesions*. Journal of Clinical Investigation, 1997. **100**(11): p. 2680-2690.
49. Gonzalez-Quesada, C. and N.G. Frangogiannis, *Monocyte Chemoattractant Protein (MCP-1)/CCL2 as a biomarker in Acute Coronary Syndromes*. Current atherosclerosis reports, 2009. **11**(2): p. 131-138.
50. ThermoFisher Scientific. *CCL2 / MCP-1 Antibody (29H86L56), ABfinity™ Rabbit Monoclonal*. Available from: <https://www.thermofisher.com/order/genome-database/antibody/CCL2-MCP-1-Antibody-clone-29H86L56-Monoclonal/700489>.
51. Joris, I., E. Stetz, and G. Majno, *Lymphocytes and monocytes in the aortic intima--An electron-microscopic study in the rat*. Atherosclerosis, 1979. **34**(3): p. 221-31.
52. ScienCell Research Laboratories. *Human Coronary Artery Endothelial Cells*. Available from: <http://www.sciencellonline.com/products-services/primary-cells/human-coronary-artery-endothelial-cells.html>.
53. Harvey, K.A., et al., *Oleic acid inhibits stearic acid-induced inhibition of cell growth and pro-inflammatory responses in human aortic endothelial cells*. Journal of Lipid Research, 2010. **51**(12): p. 3470-3480.

54. He, J., et al., *Role of mitochondrial cytochrome c in cocaine-induced apoptosis in coronary artery endothelial cells*. J Pharmacol Exp Ther, 2000. **295**(3): p. 896-903.
55. Staiger, H., et al., *Palmitate-induced interleukin-6 expression in human coronary artery endothelial cells*. Diabetes, 2004. **53**(12): p. 3209-16.
56. Karimi, A., et al., *Measurement of the uniaxial mechanical properties of healthy and atherosclerotic human coronary arteries*. Mater Sci Eng C Mater Biol Appl, 2013. **33**(5): p. 2550-4.
57. Armentano, R.L., et al., *Arterial wall mechanics in conscious dogs. Assessment of viscous, inertial, and elastic moduli to characterize aortic wall behavior*. Circ Res, 1995. **76**(3): p. 468-78.
58. Perry, R., et al., *Coronary artery wall thickness of the left anterior descending artery using high resolution transthoracic echocardiography--normal range of values*. Echocardiography, 2013. **30**(7): p. 759-64.
59. Bertaso, A.G., et al., *Epicardial fat: definition, measurements and systematic review of main outcomes*. Arq Bras Cardiol, 2013. **101**(1): p. e18-28.
60. Duchesne, M.J., et al., *A rapid method for converting medical Computed Tomography scanner topogram attenuation scale to Hounsfield Unit scale and to obtain relative density values*. Engineering Geology, 2009. **103**(3-4): p. 100-105.
61. Marcus, F.I., A. Nava, and G. Thiene, *Arrhythmogenic RV Cardiomyopathy/Dysplasia: Recent Advances*. 2007: Springer Milan.
62. Hinghofer-Szalkay, H. and J.E. Greenleaf, *Continuous monitoring of blood volume changes in humans*. J Appl Physiol (1985), 1987. **63**(3): p. 1003-7.
63. Chandler, W.L. and G. Schmer, *Evaluation of a new dynamic viscometer for measuring the viscosity of whole blood and plasma*. Clin Chem, 1986. **32**(3): p. 505-7.
64. Anderson, H.V., et al., *Coronary artery flow velocity is related to lumen area and regional left ventricular mass*. Circulation, 2000. **102**(1): p. 48-54.
65. Dole, W.P., et al., *Diastolic coronary artery pressure-flow velocity relationships in conscious man*. Cardiovasc Res, 1984. **18**(9): p. 548-54.
66. Mukherjee, D., et al., *Cardiovascular Catheterization and Intervention: A Textbook of Coronary, Peripheral, and Structural Heart Disease*. 2010: CRC Press.

